https://doi.org/10.5194/egusphere-2026-3509
Preprint. Discussion started: 27 July 2026

Quantifying the difference between methodologies for locating the Asian Summer Monsoon Anticyclone boundary and position

Oleh Kachula[1], Bärbel Vogel[1], Gebhard Günther[1], Rolf Müller[1], and Felix Ploeger[1,2]

[1]Institute of Climate and Energy Systems (ICE-4), Forschungszentrum Jülich, Jülich, Germany
[2]Institute for Atmospheric and Environmental Research, University of Wuppertal, Wuppertal, Germany

Correspondence: O. Kachula (o.kachula@fz-juelich.de)

Abstract.

Locating the boundary of the Asian summer monsoon anticyclone (ASMA) in the upper troposphere-lower stratosphere (UTLS) (350 K-410 K potential temperature) is important to analyze the transport of pollutants by the ASMA into the stratosphere. The definition of the ASMA boundary highly impacts the information about the anticyclone's behavior and affects conclusions on its spatio-temporal variability in particular regarding trends. Here, we quantify the differences between methodologies based on potential vorticity (PV) and the Montgomery streamfunction (MSF) used to determine the location of the ASMA boundary for July and August 2023 at 380 K. In addition, we apply the unsupervised machine learning spectral clustering method which combines both PV and MSF fields to derive the location of the boundary. We find that the MSF-based method tends to incorporate the eastward-shed eddy over the Pacific around 140° E into the main anticyclone and is also an optimal tool for analyzing the multidecadal evolution of the ASMA, particularly on sub-daily time scales. The PV-based methodology is better suited when temporal averaging is acceptable, as it facilitates a cleaner separation of the main ASMA body from the shed eddies. Spectral clustering, however, can exhibit either behavior during the season. Finally, we compare the derived boundaries with satellite measurements of carbon monoxide, showing that the PV-based and MSF-based methodologies successfully enclose the core of elevated carbon monoxide levels as effectively as the spectral clustering method.

1 Introduction

The Asian summer monsoon anticyclone (ASMA) is the dominant upper troposphere-lower stratosphere (UTLS) meteorological circulation pattern in the Northern Hemisphere during boreal summer (e.g., Mason and Anderson 1963; Randel and Park 2006; Park et al. 2007; Manney et al. 2021). The anticyclone zonally varies in the East-West direction covering the area from East Africa to the western Pacific (Zarrin et al. 2010). The strong convection of the ASMA occurs over South and East Asia (Randel and Park 2006; Park et al. 2008). The Asian monsoon system also influences the climate of the region thus impacting the livelihood of densely populated areas like India and Southeast Asia (Bowden et al. 2023; Maiti et al. 2024; Sinha et al. 2026).

Trace gas measurements can be used to study circulation patterns in the atmosphere. Near the surface anthropogenic pollutants are being uplifted by strong upward convection in the ASMA region and trace gases such as carbon monoxide (CO) with

https://doi.org/10.5194/egusphere-2026-3509
Preprint. Discussion started: 27 July 2026

lifetimes in the range of the time scale of upward transport into the stratosphere (weeks to months) can be used to investigate the transport barrier at the edge of the ASMA. Microwave Limb Sounder (MLS) satellite measurements and in-situ measurements that provide CO molar mixing ratios at different pressure levels can be employed to study the influence of the Asian summer monsoon anticyclone on the UTLS chemical composition (Park et al. 2009; Vogel et al. 2015; Santee et al. 2017; von Hobe et al. 2021).

Determining the boundary of the ASMA is important, as tropospheric trace gases are confined to a certain extent within the anticyclone (e.g., Vogel et al. 2019; Legras and Bucci 2020; Clemens et al. 2024; Becker et al. 2025); this mechanism is noticeable both in observations and model simulations. There is some export of the ASMA air quasi-horizontally, to the east and west (e.g., Hsu and Plumb 2001; Popovic and Plumb 2001; Vogel et al. 2014; Fadnavis et al. 2018; Clemens et al. 2022; Riese et al. 2025; Vogel et al. 2026).

Despite the anticyclone being confined between strong easterlies and westerlies (Zarrin et al. 2010), it is a challenge to determine the location of a closed contour of the ASMA boundary on a range of potential temperature levels in the UTLS (Manney et al. 2021). The strong temporal variability of the ASMA makes it difficult to define the boundary on sub-daily time scales (Legras and Bucci 2020). The ASMA boundary is often diffuse making the gradients in potential vorticity (PV) at the edge very fragmented on a specific isentropic surface (Ploeger et al. 2015; Clemens et al. 2022). Small-scale eddies or ASMA bimodal or trimodal states, when the anticyclone splits into multiple contours, require a methodology taking into account the different states of the ASMA (Zhang et al. 2002, Siu and Bowman 2020, Kachula et al. 2025). The equatorward side of the anticyclone is considered “leaky” due to deep convection over South Asia and its effect on the anticyclone circulation (Randel and Park 2006), which allows cross-barrier transport (Ploeger et al. 2015). All these challenges make a universally applicable method for locating the boundary of the ASMA difficult to develop.

During last decades a comprehensive set of methodologies was developed to define the edge of the ASMA (Garny and Randel 2013; Ploeger et al. 2015; Legras and Bucci 2020; Manney et al. 2021; Musaid et al. 2024; Kachula et al. 2025), its center and other spatio-temporal characteristics. The methodologies are based on geopotential height (GPH) (Zhang et al. 2002; Zarrin et al. 2010; Nützel et al. 2016; Musaid et al. 2024), potential vorticity (Garny and Randel 2013; Ploeger et al. 2015; Clemens et al. 2022), the Montgomery streamfunction (MSF) on isentropic surfaces (Popovic and Plumb 2001, Santee et al. 2017, Manney et al. 2021, Kachula et al. 2025), Lagrangian trajectories (Legras and Bucci 2020), zonal and meridional wind components (Zhang et al. 2002; Musaid et al. 2024), and combinations of the above and additional physical quantities, e.g., zonal wind and relative vorticity (Siu and Bowman 2020).

Zhang et al. (2002) define a line between the easterlies and westerlies located at the minimum of the absolute zonal wind on isobaric surface as the ridge line. Then the center of the ASMA is determined as the position along the ridge line where the geopotential height is maximum. This definition is also used by Zarrin et al. (2010) and Nützel et al. (2016).

Musaid et al. (2024) determine the edge of the ASMA by calculating the climatological mean GPH value (for July and August 2005-2023) and selecting the first outer closed contour inside a predefined region (20° S – 70° N, 30° W – 160° E). Musaid et al. (2024) acknowledge that fixing a single GPH value might not be useful on shorter time scales (e.g., daily), therefore they

https://doi.org/10.5194/egusphere-2026-3509
Preprint. Discussion started: 27 July 2026

propose to select different GPH contour values based on the location of the wind speed maximum of the westerlies over the subtropics and easterlies over the tropics on an isobaric surface.

Garny and Randel (2013) demonstrate that trace gas confinement withing the ASMA core correlates well with PV contours, though they found it challenging to dynamically locate a precise transport barrier. Ploeger et al. (2015) defined the ASMA boundary by calculating a smoothed PV on a specific isentropic surface (e.g., 380 K) and locating the maximum PV gradient as a function of monsoon-centered equivalent latitude. Because the ASMA is bounded to the north by the subtropical westerly jet, this methodology carefully distinguishes between the maximum PV gradient marking the anticyclone boundary and strong PV gradients associated with the jet core.

Santee et al. (2017) choose a specific ASMA region (15° N – 45° N, 45° E – 90° E) where the MSF and wind speed values are used in a linear fit for selected isentropes in June. The MSF values for the ASMA boundary are then derived from the linear fit at wind speeds of 10 m s^{-1} at 370 K and 390 K and 5 m s^{-1} at 350 K and 410 K. Then the climatological MSF contour for each isentrope is calculated by averaging the 10 years of the MSF values from the linear fit. The same climatological MSF contour values are used by Manney et al. (2021).

Kachula et al. (2025) use the absolute vortex moment definition (Matthewman et al. 2009) and introduce an optimization technique to derive the MSF contour value at the edge of the ASMA (i.e., at the location of the transport barrier) for a specific point in time on isentropic surfaces. The advantage of this method is that it can be applied at any time scale, allowing the selection of individual days (hours), as well as mean values over one monsoon season and even over many years or decades.

Many of the methodologies rely on finding maximum/minimum or some unique characteristic of a physical quantity which can be distinguished from the surrounding of the ASMA. This provides an opportunity to apply unsupervised machine learning techniques like clustering to be able to split the values of MSF, PV or GPH on different groups with the expectation of determining the edge of the ASMA (von Luxburg 2007). The spectral clustering method is useful for grouping non-convex data structures by targeting the graph partition problem. It starts by constructing the similarity matrix (the radial basis function (RBF) or Gaussian kernel) and performing eigenvalue decomposition on the resulting Laplacian matrix. The method then identifies a lower-dimensional embedding that approximates the best graph cut where clusters become linearly separable. Thus, spectral clustering can combine different physical quantities that were previously used separately to define the ASMA boundary.

Here, we quantify the difference between a variety of methodologies used to calculate the boundary of the Asian summer monsoon anticyclone and to define its center (or multiple centers). Some of the methods require climatological data to derive the ASMA contour, while for some it is possible to work on sub-daily time scales. We compare only methods that allow the calculation of the ASMA boundary using meteorological data; here, we use ERA5 reanalysis (Hersbach et al. 2020) provided by the European Centre for Medium-Range Weather Forecasts (ECMWF) for the year 2023. Methodologies that require additional calculations (e.g., for Lagrangian trajectories) are not considered here.

https://doi.org/10.5194/egusphere-2026-3509
Preprint. Discussion started: 27 July 2026

2 Data description and selected methodologies

To compare different methodologies we employ the ERA5 reanalysis that has about 31 km ($0.3^\circ \times 0.3^\circ$) horizontal resolution; here we use high horizontal resolution ERA5 data $1^\circ \times 1^\circ$ at noon (12:00 UTC) as a source of geopotential, PV, temperature, zonal and meridional wind components. The Montgomery streamfunction (for its definition see below) is then calculated using temperatures and geopotential on a specific isentropic surface from the ERA5 dataset. We select July and August 2023 at 380 K in this work and provide daily and seasonal mean results. We utilize a $1^\circ \times 1^\circ$ horizontal resolution because the spectral clustering algorithm is memory-intensive and computationally demanding. Comparison tests using higher horizontal resolutions (e.g., $0.3^\circ \times 0.3^\circ$) provided consistent results, justifying this choice.

We compare the Asian summer monsoon anticyclone's edge location, centroid position and area based on three distinct methodologies. These include the PV-based approach (Ploeger et al. 2015), hereafter termed the PV-gradient method; the MSF-based approach (Kachula et al. 2025), hereafter termed the MSF-background method; and the unsupervised machine learning spectral clustering method, hereafter termed the SC method, which combines both the PV and MSF fields on an isentropic surface.

The vertical component of Ertel's PV is defined in an isentropic coordinate system as follows:

$$\mathrm{PV} = -g\frac{dp}{d\theta}(\zeta + 2\Omega\sin\phi), \tag{1}$$

where p is pressure, ϕ is latitude, g is acceleration due to gravity, ζ is the relative vorticity and Ω is the rotation frequency of the Earth. Ploeger et al. (2015) calculate the edge of the ASMA at the location of the maximum of the PV gradient with respect to a monsoon-centered equivalent latitude using a time-averaged PV field over variable number of days (Algorithm A1). Ploeger et al. (2015) utilize a variable-day running mean to smooth the PV field. In this work, we apply a time window of ± 1 day for the majority of time-points in July and August 2023. For 14 of the 62 days, a ± 2 or ± 3 day window is applied. Additionally, for six days in August 2023 (9-13 and 16 August), the PV-barrier could not be identified, and these time points are excluded from the analysis. Employing a fixed time window for the majority of the days ensures an objective treatment of the season, simplifying calculations while providing a close approximation of the original approach.

The Montgomery streamfunction describes the geostrophic flow on isentropic surface and is defined as:

$$\mathrm{MSF} = c_p T + gz, \tag{2}$$

where, c_p is the specific heat capacity at constant pressure, T is temperature on the isentropic surface, g is gravitational acceleration and z is geopotential height on an isentropic surface. Thus, MSF combines potential energy and thermal energy of the air. The methodology of Kachula et al. (2025) defines an ASMA box that divides the horizontal grid into two regions: grid points inside and outside the box. Next, a non-negative real number, termed the background value, is subtracted from MSF values at the specific time point and isentropic surface. The resulting values are clipped to zero (ensuring that no negative values remain) and denoted as the residual Montgomery streamfunction. Kachula et al. (2025) state that the optimized background value, which also serves as the contour value defining the ASMA boundary, can be calculated by maximizing the ratio of the residual Montgomery streamfunction values inside the ASMA box to those outside the box (Algorithm A2).

https://doi.org/10.5194/egusphere-2026-3509
Preprint. Discussion started: 27 July 2026

There is no ground truth which allows the edge of the Asian summer monsoon anticyclone for a specific point in time to be determined. This leads to a diverse set of methodologies to work around this issue. In addition to the existing methodologies (e.g., Ploeger et al. 2015; Kachula et al. 2025), we further provide the spectral clustering method, a technique that takes into account MSF and PV fields (we use here the time-averaged PV field same as for Ploeger et al. (2015) methodology) together and clusters each grid cell based on their similarity (Algorithm B1). The geopotential is not included as an additional feature in the spectral clustering method because it is already accounted for in the calculation of the MSF field (see Eq. 2).

We calculate the ASMA centroid position by utilizing its boundary which can be represented as a polygon with vertices at certain grid points. The polygon's vertices have longitudinal and latitudinal coordinates which can be averaged to retrieve the polygon center. This method does not take into account the values that are located inside of the boundary, so if they are unevenly distributed our centroid position can diverge from the center of mass but still can be used as a metric to analyze the position of the ASMA contour when applied to all methodologies.

As we mentioned earlier the ASMA can be in so called bi- or trimodal states. There are multiple definitions for these states. For example, Nützel et al. (2016) calculates the centroid position for multiple years and then look at its distribution – if the values are grouped around two or more positions they considered as bimodal state of the anticyclone. Siu and Bowman (2020) and Kachula et al. (2025) instead look at simultaneous contours (centers) of the ASMA. To simplify our analysis, this work considers only a single anticyclone center. Even if the boundary value of PV or MSF highlights multiple contours, smaller structures are removed during postprocessing. Additionally, for 1-4 July 2023, a specific filter was applied to isolate the main contour from the surrounding environment. Considering only a single ASMA center might slightly bias the position of the ASMA but as shown in Kachula et al. (2025) the number of days where the anticyclone has multiple centers simultaneously has decreased in the 2020s compared to the 1980s.

To conduct the boundary comparison we utilize the Jaccard index which provides a simple metric to judge the overlapping of polygons and hence their similarity. The index takes values between $[0,1]$, where the low values show weak similarity between polygons and high values show strong similarity (e.g., 1 is for identical polygons.) The Jaccard index is defined as follows:

$$J(A,B) = \frac{|A \cap B|}{|A \cup B|}, \tag{3}$$

where A and B are two polygons that represent the ASMA boundaries for different methodologies, and $|X|$ denotes the number of grid points inside of a polygon X.

3 Results from different methodologies

In this work we provide a quantitative comparison between different methodologies that define the edge of the ASMA. First, we describe several scenarios of how the boundaries are positioned on a horizontal grid. Then we provide the analysis based on two months: July and August (the core season of the Asian summer monsoon) of 2023. The time-series will give an insight on the spatio-temporal evolution of the boundary's center along latitudinal and longitudinal directions. Also, we investigate how boundaries that define the edge of the ASMA according to the PV-gradient, MSF-background and SC methods, as described in Section 2, overlap pairwise during the same season and what area they cover.

https://doi.org/10.5194/egusphere-2026-3509
Preprint. Discussion started: 27 July 2026

Figure 1 shows horizontal plots with ASMA boundaries as defined by different methodologies, illustrating several scenarios of boundary shapes.

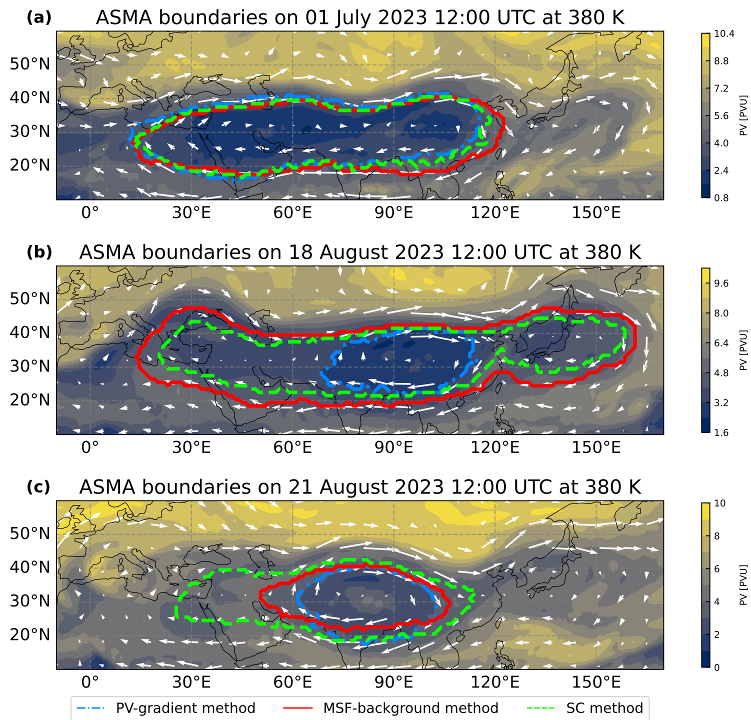

Figure 1. ASMA boundaries calculated by using the PV-gradient (dash-dot blue line), MSF-background (solid red line) and SC (dashed green line) methods on (a) 01 July 2023, (b) 18 August 2023 and (c) 21 August 2023 at 380 K potential temperature, where the color map represents the potential vorticity (PV) field and white arrows represent the wind velocity.

In Figure 1a, the boundaries on 1 July 2023 (12:00 UTC) are positioned in the same region and show good agreement with each other, especially at their northern and southern edges. The MSF-background and SC methods provide a contour that stretches slightly further east and south-east compared to the PV-gradient method. Figure 1b shows that the eastward-shed eddy above the Pacific between 120° E and 150° E is treated differently by the various methodologies. The main challenge is to determine whether this vortex is still part of the ASMA anticyclone, or if it has already split and should be treated as a separate atmospheric circulation. On 18 August 2023 at 380 K, the MSF-background and SC methods still include the vortex as a part of the anticyclone, but the PV-gradient method excludes it from the main boundary. In Supplement 1, it is shown that the SC methods can also sometimes provide a separate contour for the vortex, while the MSF-background method tend to incorporate it to the main contour. Because this impacts the calculation of the centroid position, in this work we only take into account the main part of the anticyclone and filter out small vortices (also called eddies). Figure 1c shows a case where the PV-gradient and MSF-background methods capture a smaller atmospheric circulation compared to the SC method, which encloses a larger area

https://doi.org/10.5194/egusphere-2026-3509
Preprint. Discussion started: 27 July 2026

in the east-west direction. There is also a difference in the location of the southern edge: the PV-gradient and the SC methods show good agreement with each other, while the southern edge for the MSF-background method is shifted slightly northward.

Overall, Figures 1b and c highlight the outlier cases; however, for the majority of days during July and August 2023 all three methodologies agree on the position of the ASMA as shown in Figures 2 and 3. Analysis of the horizontal maps (Figure 1 and Supplement 1) demonstrates that the PV-gradient and MSF-background methods, alongside the SC method (which accounts for both MSF and PV fields), agree well when defining both the northern and southern edges of the ASMA in most cases, with only minor disagreements regarding the placement of the eastern and western boundaries.

Figure 2 shows the time-series of the ASMA centroid latitude position for July and August 2023 at 380 K according to the PV-gradient, MSF-background, and SC methods.

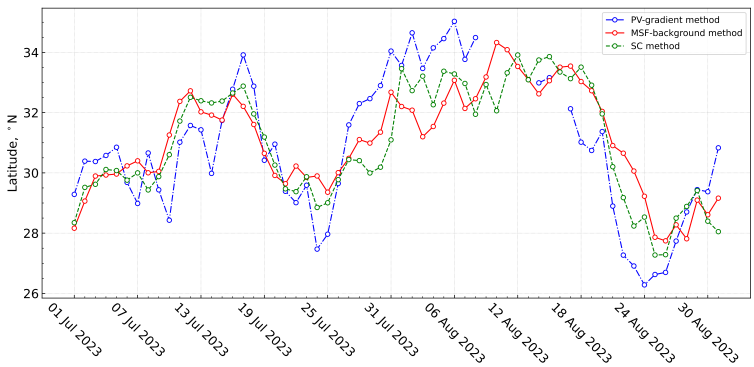

Figure 2. The centroid latitude (in ° N) time-series of the ASMA position for the PV-gradient (dash-dot blue line), MSF-background (solid red line) and SC (dashed green line) methods during July and August 2023 at 380 K potential temperature.

The MSF-background and SC methods are both based on the MSF field (the SC method also incorporates the PV field) and show little difference during July and August 2023, except for the first week of August, when the difference in centroid latitude is approximately 1°. Both methods differ slightly from the results of the PV-gradient method, in which the ASMA centroid is shifted equatorward during the second week of July. It then shifts slightly northward between 26 July and 8 August, before returning to a position closer to the equator than in the MSF-background and SC methods by roughly 3°. Overall, the differences in the centroid latitude of the ASMA boundaries remain minor throughout the entire season.

Figure 3 shows the time-series of the ASMA centroid longitude position for July and August 2023 at 380 K for the PV-gradient method (Ploeger et al. 2015), the MSF-background method (Kachula et al. 2025) and the SC method (PV- and MSF-based). Consistent with the centroid latitude, all methods agree on the centroid longitude position toward the end of the season, except for a week between 8 and 15 August when the PV-gradient method could not determine the ASMA boundary. The PV-gradient method produces several outliers in the ASMA centroid longitude due to the inherent noise in the PV field.

Figures 2 and 3 show time-series of the ASMA centroid latitude and longitude position respectively for the PV-gradient, MSF-background, and SC methods. In addition, Figure 4 illustrates the distribution of the centroid position across the three methodologies. The centroid latitude (Fig. 4, left panel) is distributed between 26° N and 35° N with all three methods iden-

https://doi.org/10.5194/egusphere-2026-3509
Preprint. Discussion started: 27 July 2026

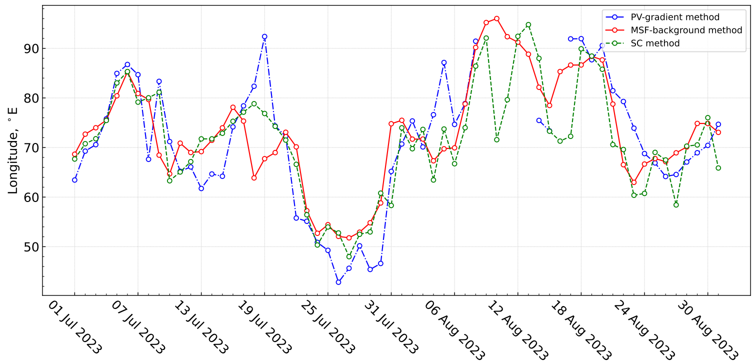

Figure 3. The centroid longitude (in ° E) time-series of the ASMA position for the PV-gradient (dash-dot blue line), MSF-background (solid red line) and SC (dashed green line) methods during July and August 2023 at 380 K potential temperature.

tifying 30° N and 33° N as the positions of the highest frequency during July and August 2023. Figure 4 (right panel) shows the distribution of the centroid longitude, where all three methods identify the location around 70° E as the dominant position of the ASMA. The statistical definition of the ASMA bimodality – where the ASMA centroid longitude resides in multiple highly pronounced locations during multi-decadal analysis (e.g., Nützel et al. 2016) – also emerge in Fig. 4 (right panel). An additional peak appears near 55° E during July and August 2023; however, this occurs rarely due to the single-year scope of our analysis. Finally, frequencies around 90° E correspond to the eastward-shed eddy over the Pacific that impacts the calculation of the centroid.

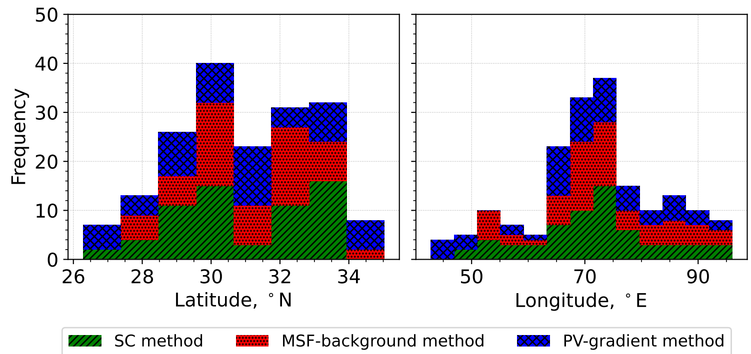

Figure 4. Distribution of the ASMA centroid latitude (left) and longitude (right) positions for the PV-gradient (blue bars with crosses), MSF-background (red bars with dots) and SC (green bars with diagonal lines) methods during July and August at 380 K potential temperature.

In summary, all three methodologies discussed here reliably determine the seasonal ASMA centroid position. Table 1 lists the mean July and August 2023 centroid coordinates for each method. The PV-gradient and SC methods (PV- and MSF-based) exhibit the greatest agreement, with a longitudinal discrepancy of at most 0.5° and almost identical in latitudes. The

https://doi.org/10.5194/egusphere-2026-3509
Preprint. Discussion started: 27 July 2026

Methodology	Latitude [° N]	Longitude [° E]
PV-gradient method	30.8 ± 2.3	71.0 ± 12.7
MSF-background method	31.1 ± 1.7	73.2 ± 10.8
SC method	31.0 ± 1.9	71.5 ± 10.7

Table 1. Mean July and August 2023 centroid position for different methodologies at 380 K potential temperature.

centroid position according to the MSF-background method is shifted slightly eastward by approximately 2.2° compared to the PV-gradient method, 1.7° compared to the SC method, though its latitude remains almost unchanged (differing by just $\sim 0.1° - 0.3°$). Notably, the MSF-background method features the lowest standard deviation along the latitudinal axis, and the SC features the lowest along the longitudinal axis.

Figure 5 presents a time-series of the ASMA area (in fraction of the hemisphere) for July and August 2023, derived by projecting the boundary onto the Earth's surface. The SC method shows smaller day-to-day variations in area compared to the PV-gradient and MSF-background methods. The last two methods highlight a decrease in the ASMA area toward the end of July: the PV-gradient method provides a value around 3 % and the MSF-background method approaches 5 %. In contrast to the centroid position, the ASMA area exhibits greater variation among the methods. However, this divergence is less pronounced in the beginning of July 2023 (especially for the MSF-background and the SC methods) than in period between 12 and 24 August 2023, when the primary disagreement arises from the differing treatments of the eastward-shed eddy over the Pacific.

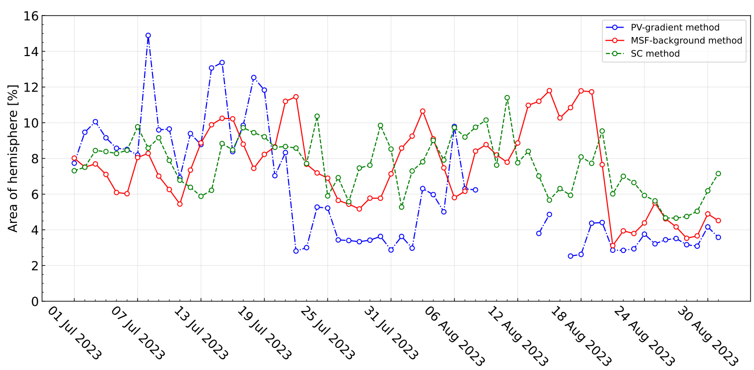

Figure 5. The ASMA area (in fraction of the hemisphere) time-series for the PV-gradient (dash-dot blue line), MSF-background (solid red line) and SC (dashed green line) methods during July and August 2023 at 380 K potential temperature.

To quantify the spatial agreement among the deduced ASMA boundaries, we employ the Jaccard index. Figure 6 presents the degree of overlap between the polygons representing the anticyclone boundaries (where a value of 1 indicates identical boundaries and 0 indicates no overlap). From the beginning of July 2023 until around 22 July 2023, the PV-gradient, MSF-background and SC methods show good agreement, with Jaccard indices rarely dropping below 0.65. Between 22 July and 15 August, however, overall agreement worsens because of the discrepancies between PV-gradient and MSF-background ap-

https://doi.org/10.5194/egusphere-2026-3509
Preprint. Discussion started: 27 July 2026

proaches. During this period, the MSF-background and SC methods still maintain a moderate-to-high Jaccard index (0.55 to 0.9). From 22 August onward, all index values rebound because all three methodologies exclude the eastward-shed eddy over the Pacific from the main contour.

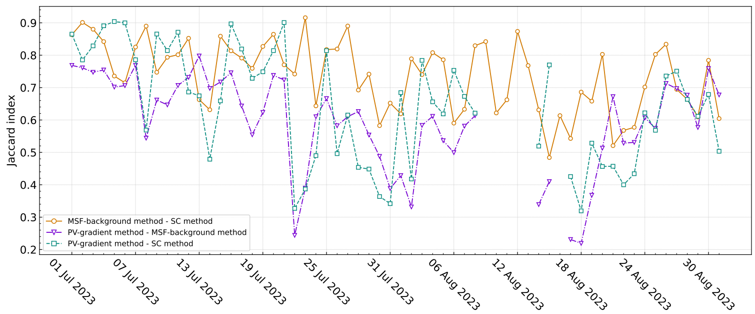

Figure 6. Time series for July and August 2023 of the Jaccard index, calculated pairwise for two methods to quantify the differences between ASMA boundaries derived from different methodologies at 380 K potential temperature.

Figure 7 presents a statistical summary of all Jaccard indices, demonstrating that for the majority of cases during July and August 2023 at 380 K the index is above 0.6 (especially for the MSF background-SC methods), with a mean of approximately 0.7.

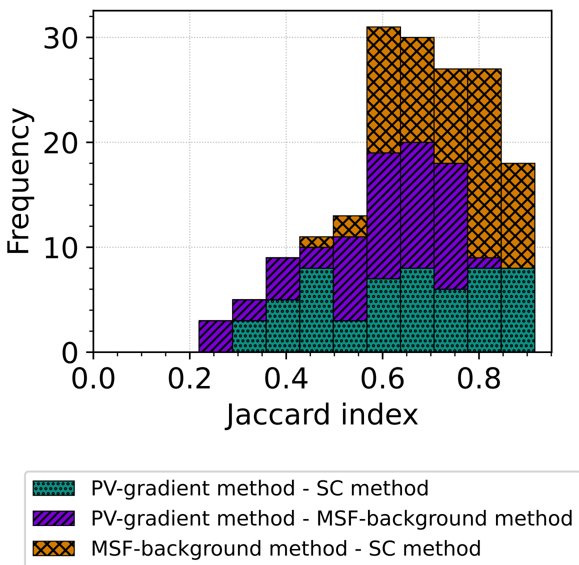

Figure 7. Distribution of the Jaccard indices, calculated pairwise for two methods to quantify the differences between ASMA boundaries derived from different methodologies at 380 K.

https://doi.org/10.5194/egusphere-2026-3509
Preprint. Discussion started: 27 July 2026

4 Comparison with satellite measurements

To evaluate how well the ASMA boundary and position determined by the different methodologies agree with satellite measurements, we use carbon monoxide (CO) observations from the Microwave Limb Sounder (MLS). Unlike nadir-viewing satellite sensors (that provide total column of a chemical tracer), the MLS has a vertical resolution that allows the molar mixing ratios of carbon monoxide within the UTLS to be deduced. The vertical resolution of MLS v5.0 CO is within 4.9–5.1 km, the horizontal resolution ranges from 400 to 570 km, and the single-profile precision is 9–16 ppbv over the 147–31 hPa pressure range (e.g., Livesey et al. 2022). The MLS CO molar mixing ratios are reported on a pressure grid but our analysis is conducted at 380 K potential temperature. Because of this we had first to select and average the air parcels in the range between 380 K $\pm$ 5 K and then interpolate the two month measurements (July and August 2023) on a horizontal regular grid. Due to the MLS coverage one can not compare single days, therefore we compare mean values for July and August 2023.

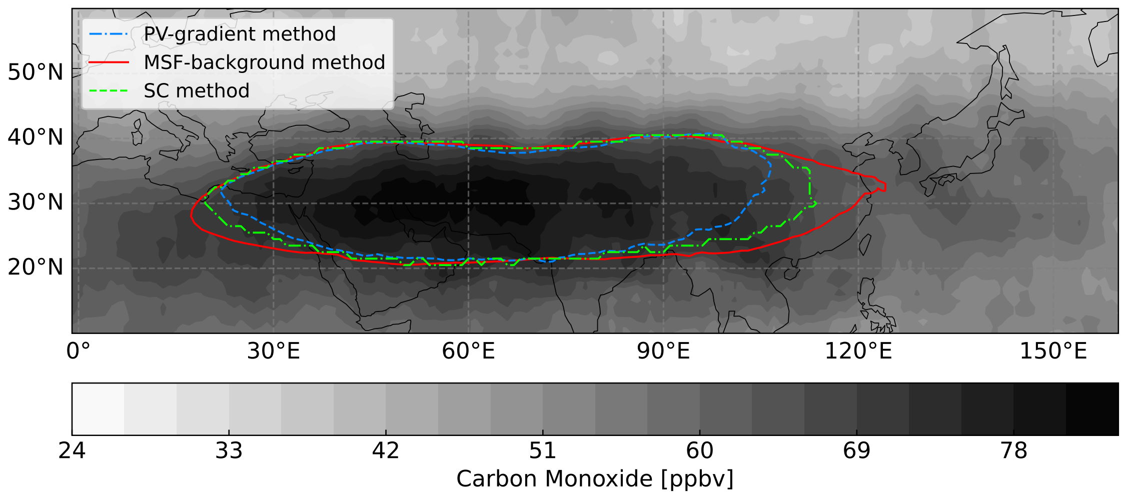

Figure 8. Horizontal map of July and August 2023 average MLS carbon monoxide molar mixing ratio (in ppbv) with ASMA boundaries for the PV-gradient (dashed blue line) and MSF-background (solid red line) and SC (dashdot green line) methods at 380 K $\pm$ 5 K.

In general, the ASMA boundary and position according to the PV-gradient, MSF-background and SC methods show a good overall agreement to the MLS CO distribution at 380 K $\pm$ 5 K (Fig. 8). Figure 8 shows that for average July and August 2023 the MSF-background method covers the greatest area, following by the SC method. The three methodologies approximate the western tail of the ASMA better than the eastern, where the MSF-background method has the greatest difference. The PV-gradient method provides the boundary that lays within the above two and covers a smaller core of the ASMA. The three methodologies show a similar behavior at the northern side of the positive CO anomaly in the monsoon core including the values that are higher than $\sim$ 70 ppbv.

https://doi.org/10.5194/egusphere-2026-3509
Preprint. Discussion started: 27 July 2026

5 Discussion and Conclusions

The assessment of the spatio-temporal evolution of the Asian summer monsoon anticyclone (ASMA) depends on the methodology that is used to determine its boundary. To reliably determine the anticyclone's edge, physical quantities such as potential vorticity and the Montgomery streamfunction are calculated from meteorological reanalyses; also satellite measurements of trace species can be used. In this work we provide a quantitative comparison of methodologies based on the work of Ploeger et al. (2015) (the PV-gradient method) and Kachula et al. (2025) (the MSF-background method) using the ERA5 reanalysis. In addition we provide a methodology based on the unsupervised machine learning spectral clustering (the SC method) analysis using the PV and MSF fields to define the anticyclone's boundary. We show daily time-series of the ASMA centroid latitude and longitude position, the ASMA area, the mean values of the centroid over July and August 2023 and time-series of the Jaccard index to highlight the degree of boundaries overlapping. Also, we compare the two month average horizontal distribution of carbon monoxide measured by MLS with boundaries of the above mentioned methodologies. The main findings are:

- The PV-gradient, MSF-background, and SC methods provide a similar centroid latitudinal and longitudinal position of the ASMA throughout July and August 2023 on 380 K.
- All three methodologies show good agreement in ASMA area, while the SC method shows smaller day-to-day variation compared to the PV-gradient and MSF-background methods.
- There is a difference how the methodologies highlight the eastward-shed eddy over the Pacific (an example of such an eddy was investigated during August 2023). While the MSF-background method assigns it to the main anticyclone, the PV-gradient method excludes it from the main contour. The SC method can exhibit either behavior throughout July and August 2023.
- The Jaccard index for all three methodologies rarely drops below 0.5, while in July 2023 it usually stays above 0.7. The MSF-background and SC methods provide the highest degree of boundary overlap during July and August 2023, especially in July, while the Jaccard indices for the PV-gradient method show several outliers.

In this work, the methodologies of Ploeger et al. (2015) and Kachula et al. (2025) for locating the ASMA boundary are used, both of which operate specifically on isentropic surfaces. While methodologies designed for isobaric surfaces also exist (e.g., Zhang et al. 2002; Musaid et al. 2024), comparing the ASMA boundary retrieved from isobaric and isentropic surfaces is not useful and leads to biased results. Isentropic surfaces are not parallel to isobaric surfaces. Figure 9 shows a longitude-theta cross-section where the white lines correspond to the pressure levels. The 380 K potential temperature surface used in this study crosses several pressure levels; consequently, methodologies that encircle the anticyclone on a constant pressure level will capture the ASMA boundary across different potential temperature ranges, leading to a distorted comparison.

There is also a distinct difference in the spatial distribution of GPH between isobaric and isentropic surfaces: the former provides generally smooth GPH fields, while the latter contains small, localized maxima of high values. These are considered noise and complicate the retrieval of a continuous, closed contour on sub-daily time-scales.

https://doi.org/10.5194/egusphere-2026-3509
Preprint. Discussion started: 27 July 2026

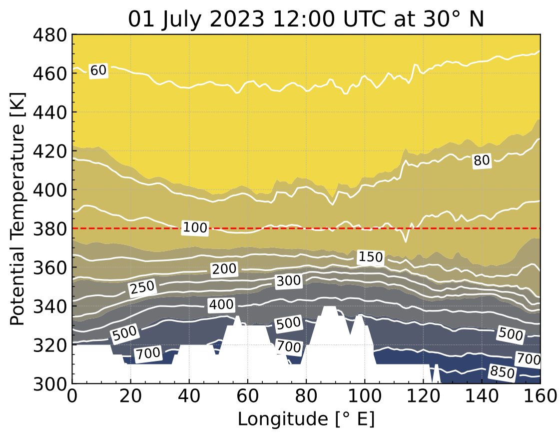

Figure 9. Longitude-theta cross sections at 30° N on 1 July 2023 of the geopotential (colormap) and pressure levels in hPa (solid white lines) from the ERA5 reanalysis dataset. Dashed red line is 380 K potential temperature.

Although applying the spectral clustering method to the ASMA meteorological data can be computationally intensive, it provides valuable insights into the coupled distribution of the PV and MSF fields. The PV-gradient method can be used to clearly separate the anticyclone from smaller-scale eddies shed. The MSF-background method provides a good approximation of the ASMA boundary and shows a good overall agreement with the PV-gradient and SC methods but in contrast to the PV-gradient method can work on sub-daily time scales and larger range of potential temperatures. This work shows that depending on the initial conditions and the target of the study, each methodology has its own advantage: the MSF-background method is useful for multidecadal analysis of the ASMA, PV-gradient method can focus on the anticyclone's core when smoothed PV-fields are available and SC method is a valuable tool for highlighting the ASMA barrier location from the underlying clustering patterns at a specific point in time.

Code availability. The Jupyter notebook containing the code for this project is available at https://jugit.fz-juelich.de/o.kachula/asma-difference

Data availability. The ERA5 data used here are available from the ECMWF (`https://www.copernicus.eu/en`).

Author contributions. The study was conceived by OK, BV, GG, RM, and FP. OK and FP designed the methods and conducted calculations for this study. BV directed the structure of the paper, analysed the calculated results, and supported the study. GG and RM provided advice and guidance for the analysis of the methods comparison. The results were discussed by all the co-authors. The paper was written by OK with contributions from all the co-authors.

https://doi.org/10.5194/egusphere-2026-3509
Preprint. Discussion started: 27 July 2026

Competing interests. At least one of the (co-)authors is a member of the editorial board of Atmospheric Chemistry and Physics. Otherwise there are no competing interests.

Acknowledgements. We thank the European Centre for Medium-Range Weather Forecasts (ECMWF) for providing the ERA5 reanalyses and the Jülich Supercomputing Centre (JSC; Research Centre Jülich, Germany) for the storage resources on the MeteoCloud data archive. The presented work were mainly funded by the German Science Foundation (Deutsche Forschungsgemeinschaft, DFG) as part of the HALO Priority Program SPP 1294 (project VO 1276/7-1) and of the TRR 301 (project ID 428312742). We would like to sincerely thank Susann Tegtmeier (University of Saskatchewan) for helpful discussions.

Appendix A: Algorithms of the PV-gradient and MSF-background methods

Algorithm A1 PV-gradient method: the definition of the ASMA edge based on Ploeger et al. (2015)

Require: Time-averaged potential vorticity grid PV, latitudes ϕ, longitudes λ, peak prominence p, edge buffer b

Compute grid cell area matrix: $A_{i,j} \leftarrow R^2_{\text{Earth}} \cos(\phi_i) \cdot \Delta\phi \cdot \Delta\lambda$
Flatten PV and A into 1D vectors **pv** and **a**
Define new PV axis $P \leftarrow \{-2.0, -1.8, \ldots, 10.0\}$
for each $t_i \in P$ **do**
    Compute cumulative area: $A_{cum}[i] \leftarrow \sum_{\{m|\mathbf{pv}_m \leq t_i\}} \mathbf{a}_m$
end for
Compute eq.-lat.: $\Phi = \arcsin\left(1 - A_{cum}/(2\pi R^2_{\text{Earth}})\right) \times 180/\pi$
Calculate the gradient $G \leftarrow \frac{dP}{d\Phi}$ and smooth it.
Define search domain: $\Omega \leftarrow \{i \mid \Phi[i] \leq 80° \wedge (2.0 \leq P[i] \leq 5.0)\}$
$idx \leftarrow \text{argmax}(-G[\Omega], p, b)$
return NaN **if** idx is NaN **else** $P[\Omega][idx]$

Appendix B: The spectral clustering method

Clustering is a data analysis approach used to assign a label to each object from a set, where objects within the same cluster exhibit high similarity and objects in different clusters exhibit low similarity. The definition of similarity is task-dependent and is determined by the user.

There is a diverse family of clustering algorithms. Some are designed for data with “flat” geometry (e.g., K-Means), while others are suited for non-linear or “non-flat” geometry (e.g., Spectral Clustering, DBSCAN). Here, “flat” and “non-flat” geometries refer to whether the data are linearly separable. In this work, while the ASMA roughly resembles an ellipsoid shape in the PV and MSF fields, its confinement by the subtropical jet to the north and the tropical jet to the south creates a complex,

https://doi.org/10.5194/egusphere-2026-3509
Preprint. Discussion started: 27 July 2026

Algorithm A2 MSF-background: the definition of the ASMA edge based on Kachula et al. (2025)

Require: $M \in \mathbb{R}^{n\times m}$ (MSF grid)
Require: $\beta := (15^\circ\ \mathrm{N} - 45^\circ\ \mathrm{N}, 45^\circ\ \mathrm{E} - 90^\circ\ \mathrm{E})$
for each $b \in \mathrm{Range}[\min(M), \max(M)]$ **do**
  $R \leftarrow M - b$
  if $R[i,j] < 0$ **then**
    $R[i,j] = 0$
  end if
  $M_{\mathrm{in}} \leftarrow \mathrm{sum}(R \in \beta)$
  $M_{\mathrm{out}} \leftarrow \mathrm{sum}(R \notin \beta)$
  $f(b) \leftarrow \frac{M_{\mathrm{in}}}{(M_{\mathrm{out}}+1)}$
end for
return Edge $\leftarrow \mathrm{argmin}(-f)$

non-linear manifold, presenting a case of "non-flat" geometry. For this specific application, the spectral clustering method proved more effective at encircling the ASMA than either DBSCAN or HDBSCAN.

Algorithm B1 illustrates a simplified variant of the spectral clustering method. We utilize the implementation provided by the free and open-source Python library scikit-learn (`sklearn.cluster.SpectralClustering`; Pedregosa et al. 2011). There are two important parameters that can be adjusted: number of clusters (NC) and the gamma parameter (γ).

Algorithm B1 ASMA Edge Detection based on the Spectral Clustering

Require: Normalized grids $\mathscr{X} = \{X_1, \ldots, X_q\} \in \mathbb{R}^{n\times m}$ and the number of clusters k.
$F \leftarrow [\mathrm{vec}(X_1); \mathrm{vec}(X_2) \ldots \mathrm{vec}(X_q);] \in \mathbb{R}^{(nm)\times q}$
$A_{ij} \leftarrow \exp(-\|F_i - F_j\|^2 / 2\sigma^2)$
$L_{sym} \leftarrow$ Compute normalized Laplacian from A
$V \leftarrow [v_1, v_2, \ldots, v_k] \in \mathbb{R}^{(nm)\times k}$ {First k eigenvectors of L_{sym}}
return Cluster labels $C \leftarrow$ K-means(V, k)

The number of clusters determines into how many distinct groups the dataset will be partitioned. Figure B1 shows how the ASMA boundary on 23 August 2023 12:00 UTC at 380 K changes depending on the number of clusters (ranging from 2 to 7). When NC = 2, the resulting clusters fail to capture the southwestern part of the boundary on this specific day; only the northern side, where the strong subtropical jet is located, can be detected. For NC = 3, the resulting clusters exhibit a finer structure for this day but still show noise on the eastern part and in general can fail to form a closed contour. For NC = 4 the main body of the anticyclone assumes a consistent and closed shape. With a larger number of clusters, the data is over-partitioned into unwanted details, highlighting the inner core of the ASMA (e.g., NC = 5, 6 and 7). For July and August 2023 at 380 K, we chose NC = 4 as a reasonable trade-off between obtaining a closed contour and minimizing the noise.

https://doi.org/10.5194/egusphere-2026-3509
Preprint. Discussion started: 27 July 2026

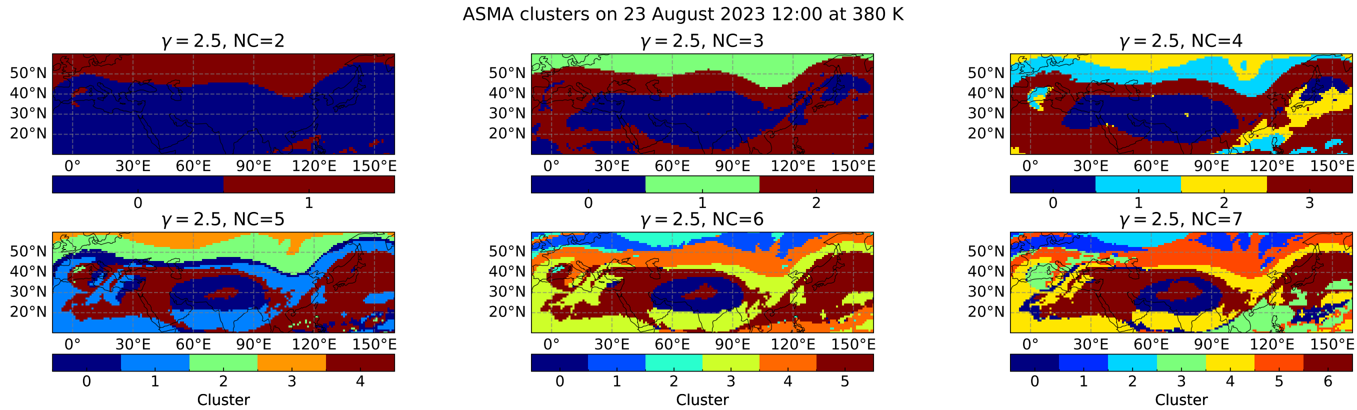

Figure B1. ASMA boundary clustered with the spectral clustering method using different number of clusters on 23 August 2023 at 380 K.

The γ parameter is used in the radial basis function (RBF) kernel, also known as the Gaussian kernel: $\exp(-\gamma||x_i - x_j||^2)$. Here, x_i and x_j are two-component vectors consisting of unit-normalized PV and MSF values at grid points i and j (the grid is flattened into a one-dimensional array). The γ parameter controls the width of the Gaussian similarity function, determining how rapidly the similarity between two objects decreases with respect to their Euclidean distance (von Luxburg 2007). Figures B2 and B3 show how the γ parameter impacts the ASMA boundary. We are interested in a continuous and smooth closed contour that is based on the PV and MSF fields at a specific point in time. The γ parameter can help reduce the noise around the boundary. As shown in Fig. B2, changing γ from 0.5 to 2.5 results in roughly the same ASMA boundary on 23 August 2023 12:00 UTC at 380 K; however, Fig. B3 illustrates that for some days, like 5 August 2023 at 380 K, a higher value of γ helps to find a closed contour and smooth the boundary. The empirical choice of $\gamma = 2.5$ for July and August 2023 at 380 K to derive the ASMA boundary agrees with methodologies of Ploeger et al. (2015) and Kachula et al. (2025).

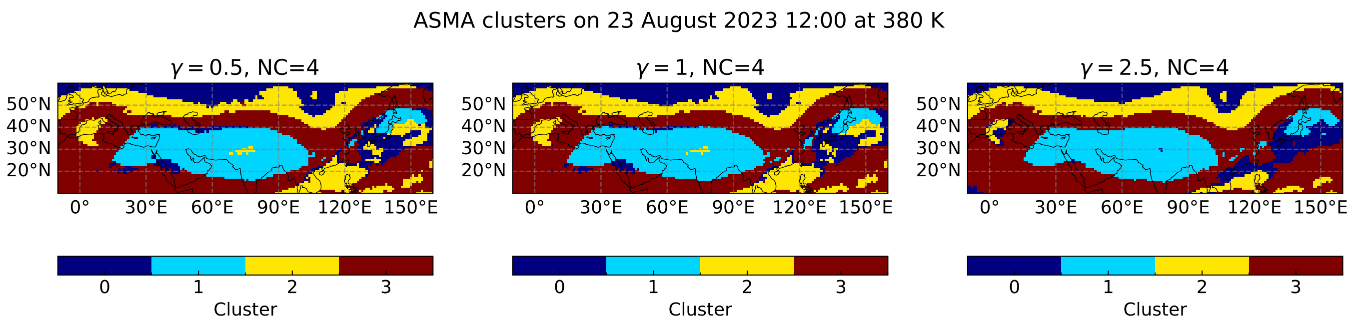

Figure B2. ASMA boundary clustered with the spectral clustering method using different values of γ on 23 August 2023 at 380 K.

https://doi.org/10.5194/egusphere-2026-3509
Preprint. Discussion started: 27 July 2026

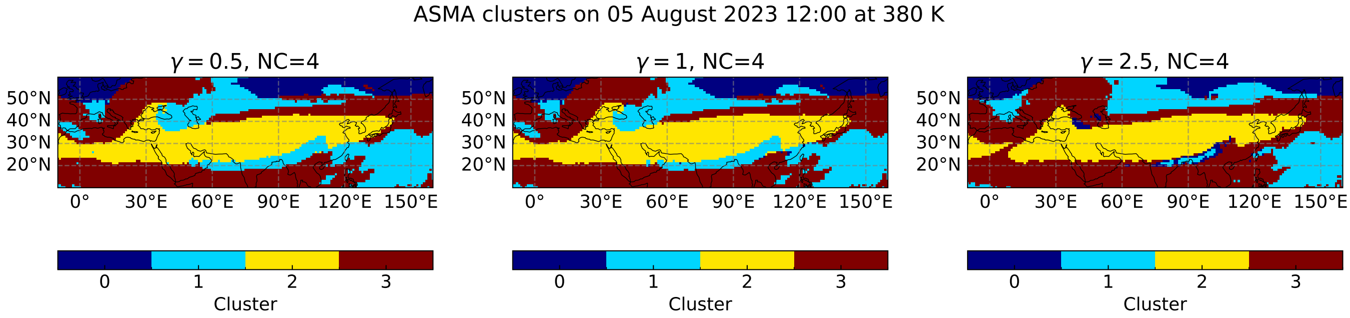

Figure B3. ASMA boundary clustered with the spectral clustering method using different values of γ on 5 August 2023 at 380 K.

References

Becker, F., Vogel, B., Günther, G., Ploeger, F., Riese, M., Rosanka, S., Taraborrelli, D., Nützel, M., Jöckel, P., Brinkop, S., and Müller, R.: Upward transport of boundary layer air to altitudes of the Asian summer monsoon anticyclone in Eulerian and Lagrangian model simulations, Meteorologische Zeitschrift, 3, 195–211, https://doi.org/10.1127/metz/1266, 2025.

Bowden, C., Foster, T., and Parkes, B.: Identifying links between monsoon variability and rice production in India through machine learning, Sci. Rep., 13, 2446, https://doi.org/10.1038/s41598-023-27752-8, 2023.

Clemens, J., Ploeger, F., Konopka, P., Portmann, R., Sprenger, M., and Wernli, H.: Characterization of transport from the Asian summer monsoon anticyclone into the UTLS via shedding of low potential vorticity cutoffs, Atmos. Chem. Phys., 22, 3841–3860, https://doi.org/10.5194/acp-22-3841-2022, 2022.

Clemens, J., Vogel, B., Hoffmann, L., Griessbach, S., Thomas, N., Fadnavis, S., Müller, R., Peter, T., and Ploeger, F.: A multi-scenario Lagrangian trajectory analysis to identify source regions of the Asian tropopause aerosol layer on the Indian subcontinent in August 2016, Atmos. Chem. Phys., 24, 763–787, https://doi.org/10.5194/acp-24-763-2024, 2024.

Fadnavis, S., Roy, C., Chattopadhyay, R., Sioris, C. E., Rap, A., Müller, R., Kumar, K. R., and Krishnan, R.: Transport of trace gases via eddy shedding from the Asian summer monsoon anticyclone and associated impacts on ozone heating rates, Atmos. Chem. Phys., 18, 11 493–11 506, https://doi.org/10.5194/acp-18-11493-2018, 2018.

Garny, H. and Randel, W. J.: Dynamic variability of the Asian monsoon anticyclone observed in potential vorticity and correlations with tracer distributions, J. Geophys. Res., 118, 13 421–13 433, https://doi.org/10.1002/2013JD020908, 2013.

Hersbach, H., Bell, B., Berrisford, P., Hirahara, S., Horànyi, A., Muñoz Sabater, J., Nicolas, J., Peubey, C., Radu, R., Schepers, D., Simmons, A., Soci, C., Abdalla, S., Abellan, X., Balsamo, G., Bechtold, P., Biavati, G., Bidlot, J., Bonavita, M., De Chiara, G., Dahlgren, P., Dee, D., Diamantakis, M., Dragani, R., Flemming, J., Forbes, R., Fuentes, M., Geer, A., Haimberger, L., Healy, S., Hogan, R. J., Hólm, E., Janiskovà, M., Keeley, S., Laloyaux, P., Lopez, P., Lupu, C., Radnoti, G., de Rosnay, P., Rozum, I., Vamborg, F., Villaume, S., and Thépaut, J.-N.: The ERA5 global reanalysis, Q. J. R. Meteorol. Soc., 146, 1999–2049, https://doi.org/10.1002/qj.3803, 2020.

Hsu, C. J. and Plumb, R. A.: Nonaxisymmetric Thermally Driven Circulations and Upper-Tropospheric Monsoon Dynamics, J. Atmos. Sci., 57, 1255–1276, 2001.

Kachula, O., Vogel, B., Günther, G., and Müller, R.: An optimization-based approach to track the Asian summer monsoon anticyclone across daily and interannual variability, Atmos. Chem. Phys., 25, 15 171–15 195, https://doi.org/10.5194/acp-25-15171-2025, 2025.

Legras, B. and Bucci, S.: Confinement of air in the Asian monsoon anticyclone and pathways of convective air to the stratosphere during the summer season, Atmos. Chem. Phys., 20, 11 045–11 064, https://doi.org/10.5194/acp-20-11045-2020, 2020.

Livesey, N. J., Read, W. G., Wagner, P. A., Froidevaux, L., Santee, M. L., Schwartz, M. J., Lambert, A., Valle, L. F. M., Pumphrey, H. C., Manney, G. L., Fuller, R. A., Jarnot, R. F., Knosp, B. W., and Lay, R. R.: Version 5.0x Level 2 and 3 data quality and description document, JPL D-105336 Rev. B, https://mls.jpl.nasa.gov/data/v5-0_data_quality_document.pdf, 2022.

Maiti, A., Hasan, M. K., Sannigrahi, S., Bar, S., Chakraborti, S., Mahto, S. S., Chatterjee, S., Pramanik, S., Pilla, F., Auerbach, J., Sonnentag, O., Song, C., and Zhang, Q.: Optimal rainfall threshold for monsoon rice production in India varies across space and time, Comm. Earth & Environ., 5, 302, https://doi.org/10.1038/s43247-024-01414-7, 2024.

Manney, G. L., Santee, M. L., Lawrence, Z. D., Wargan, K., and Schwartz, M. J.: A Moments View of Climatology and Variability of the Asian Summer Monsoon Anticyclone, J. Climate, 34, 7821 – 7841, https://doi.org/10.1175/JCLI-D-20-0729.1, 2021.

Mason, R. B. and Anderson, C. E.: The development and decay of the 100-mb. summertime anticyclone over southern Asia, Monthly Weather Review, 91, 3–12, https://doi.org/10.1175/1520-0493(1963)091<0003:TDADOT>2.3.CO;2, 1963.

Matthewman, N. J., Esler, J. G., Charlton-Perez, A. J., and Polvani, L. M.: A New Look at Stratospheric Sudden Warmings. Part III: Polar Vortex Evolution and Vertical Structure, J. Climate, 22, 1566 – 1585, https://doi.org/10.1175/2008JCLI2365.1, 2009.

Musaid, P. P., Mehta, S. K., Tegtmeier, S., Fujiwara, M., Purushotham, P., Kakkanattu, S. P., Betsy, K. B., and Seetha, C. J.: Identification of the Asian summer monsoon anticyclone based on tropical easterly and subtropical westerly jets during active and break phases, Int. J. Climatol., 44, 4260–4285, https://doi.org/10.1002/joc.8580, 2024.

Nützel, M., Dameris, M., and Garny, H.: Movement, drivers and bimodality of the South Asian High, Atmos. Chem. Phys., 16, 14 755–14 774, https://doi.org/10.5194/acp-16-14755-2016, 2016.

Park, M., Randel, W. J., Gettleman, A., Massie, S. T., and Jiang, J. H.: Transport above the Asian summer monsoon anticyclone inferred from Aura Microwave Limb Sounder tracers, J. Geophys. Res., 112, D16309, https://doi.org/10.1029/2006JD008294, 2007.

Park, M., Randel, W. J., Emmons, L. K., Bernath, P. F., Walker, K. A., and Boone, C. D.: Chemical isolation in the Asian monsoon anticyclone observed in Atmospheric Chemistry Experiment (ACE-FTS) data, Atmos. Chem. Phys., 8, 757–764, 2008.

Park, M., Randel, W. J., Emmons, L. K., and Livesey, N. J.: Transport pathways of carbon monoxide in the Asian summer monsoon diagnosed from Model of Ozone and Related Tracers (MOZART), J. Geophys. Res., 114, D08303, https://doi.org/10.1029/2008JD010621, 2009.

Pedregosa, F., Varoquaux, G., Gramfort, A., Michel, V., Thirion, B., Grisel, O., Blondel, M., Prettenhofer, P., Weiss, R., Dubourg, V., Vanderplas, J., Passos, A., Cournapeau, D., Brucher, M., Perrot, M., and Duchesnay, E.: Scikit-learn: Machine Learning in Python, Journal of Machine Learning Research, 12, 2825–2830, 2011.

Ploeger, F., Gottschling, C., Grießbach, S., Grooß, J.-U., Günther, G., Konopka, P., Müller, R., Riese, M., Stroh, F., Tao, M., Ungermann, J., Vogel, B., and von Hobe, M.: A potential vorticity-based determination of the transport barrier in the Asian summer monsoon anticyclone, Atmos. Chem. Phys., 15, 13 145–13 159, https://doi.org/10.5194/acp-15-13145-2015, 2015.

Popovic, J. M. and Plumb, R. A.: Eddy Shedding from the Upper-Tropospheric Asian Monsoon Anticyclone, J. Atmos. Sci., 58, 93–104, 2001.

Randel, W. J. and Park, M.: Deep convective influence on the Asian summer monsoon anticyclone and associated tracer variability observed with Atmospheric Infrared Sounder (AIRS), J. Geophys. Res., 111, D12314, https://doi.org/10.1029/2005JD006490, 2006.

Riese, M., Hoor, P., Rolf, C., Kunkel, D., Vogel, B., Köllner, F., Pöhlker, M., Ploeger, F., Ungermann, J., Woiwode, W., Johansson, S., Bauer, R., Barmpounis, K., Borrmann, S., Brauner, P., Clemens, J., Dragoneas, A., Ekinci, F., Emig, N., Engel, A., Eppers, O., Fadnavis, S., Friedl-Vallon, F., Geldenhuys, M., Günther, G., Grooß, J.-U., Hegglin, M. I., Hoepfner, M., Jesswein, M., Joppe, P., Kaumanns, J.,

https://doi.org/10.5194/egusphere-2026-3509
Preprint. Discussion started: 27 July 2026

Kachula, O., Keber, T., Kretschmer, E., Lachnitt, H.-C., Lauther, V., Lloyd, P. E., Molleker, S., Müller, R., Neubert, T., Ort, L., Pöschl, U., Pöhlker, C., Rapp, M., Retzlaff, M., Rhode, S., Schneider, J., Schuck, T., Sinnhuber, B.-M., Spelten, N., Strobel, J., Tomsche, L., Turhal, K., van Luijt, R., Versick, S., Voigt, C., Volk, M., von Hobe, M., Weyland, F., Zahn, A., Ziereis, H., and Zlotos, L.: Long-range transport of polluted Asian summer monsoon air to high latitudes during the PHILEAS campaign in the boreal summer 2023, Bull. Am. Meteorol. Soc., https://doi.org/10.1175/BAMS-D-24-0232.1, 2025.

Santee, M. L., Manney, G. L., Livesey, N. J., Schwartz, M. J., Neu, J. L., and Read, W. G.: A comprehensive overview of the climatological composition of the Asian summer monsoon anticyclone based on 10 years of Aura Microwave Limb Sounder measurements, J. Geophys. Res., 122, 5491–5514, https://doi.org/10.1002/2016JD026408, 2017.

Sinha, M., Jha, S., and Kumar, A.: ENSO-modulated heat source and moisture sink of Asian monsoon and its impact on rice production, Sci. Rep., 16, 10 955, https://doi.org/10.1038/s41598-026-46128-2, 2026.

Siu, L. W. and Bowman, K. P.: Unsteady Vortex Behavior in the Asian Monsoon Anticyclone, Journal of the Atmospheric Sciences, 77, 4067 – 4088, https://doi.org/10.1175/JAS-D-19-0349.1, 2020.

Vogel, B., Günther, G., Müller, R., Grooß, J.-U., Hoor, P., Krämer, M., Müller, S., Zahn, A., and Riese, M.: Fast transport from Southeast Asia boundary layer sources to northern Europe: rapid uplift in typhoons and eastward eddy shedding of the Asian monsoon anticyclone, Atmos. Chem. Phys., 14, 12 745–12 762, https://doi.org/10.5194/acp-14-12745-2014, 2014.

Vogel, B., Günther, G., Müller, R., Grooß, J.-U., and Riese, M.: Impact of different Asian source regions on the composition of the Asian monsoon anticyclone and of the extratropical lowermost stratosphere, Atmos. Chem. Phys., 15, 13 699–13 716, https://doi.org/10.5194/acp-15-13699-2015, 2015.

Vogel, B., Müller, R., Günther, G., Spang, R., Hanumanthu, S., Li, D., Riese, M., and Stiller, G. P.: Lagrangian simulations of the transport of young air masses to the top of the Asian monsoon anticyclone and into the tropical pipe, Atmos. Chem. Phys., 19, 6007–6034, https://doi.org/10.5194/acp-19-6007-2019, 2019.

Vogel, B., Lauther, V., Köllner, F., Ekinci, F., Rolf, C., Strobel, J., van Luijt, R., Volk, C. M., Borrmann, S., Dragoneas, A., Eppers, O., Molleker, S., Hoor, P., Ort, L., Weyland, F., Zahn, A., Clemens, J., Günther, G., Kachula, O., Müller, R., Ploeger, F., and Riese, M.: Continental and marine source regions contributing to the outflow of the Asian summer monsoon anticyclone during the PHILEAS campaign in summer 2023, Atmos. Chem. Phys., 26, 6283–6319, https://doi.org/10.5194/acp-26-6283-2026, 2026.

von Hobe, M., Ploeger, F., Konopka, P., Kloss, C., Ulanowski, A., Yushkov, V., Ravegnani, F., Volk, C. M., Pan, L. L., Honomichl, S. B., Tilmes, S., Kinnison, D. E., Garcia, R. R., and Wright, J. S.: Upward transport into and within the Asian monsoon anticyclone as inferred from StratoClim trace gas observations, Atmos. Chem. Phys., 21, 1267–1285, https://doi.org/10.5194/acp-21-1267-2021, 2021.

von Luxburg, U.: A tutorial on spectral clustering, Stat. Comput., 17, 395–416, https://doi.org/10.1007/s11222-007-9033-z, 2007.

Zarrin, A., Ghaemi, H., Azadi, M., and Farajzadeh, M.: The spatial pattern of summertime subtropical anticyclones over Asia and Africa: A climatological review, Int. J. Climatol., 30, 159–173, https://doi.org/10.1002/joc.1879, 2010.

Zhang, Q., Wu, G., and Qian, Y.: The Bimodality of the 100 hPa South Asia High and its Relationship to the Climate Anomaly over East Asia in Summer, J. Meteorol. Soc. Jpn., 80, 733–744, 2002.